RESEARCH PAPER

Influence of focus and deflection when comparing electron beam welds to laser welds at varying parameters in 304 SS

Joris E. Hochanadel[1] · Tate Patterson[1] · John C. Lippold[1] · Boyd Panton[1] · Matthew Q. Johnson[2] · David C. Tung[2]

Abstract

In many cases, both laser and electron beam welding may be considered for critical applications involving a wide range of structural materials. The ability to use both processes to make comparable welds in terms of both weld profile (penetration) and microstructure provides considerable process selection flexibility. In this study, autogenous, partial penetration welds on 304 and 304L SS were made using both fiber laser and electron beam processes. To simplify the analysis, many parameters were kept constant between processes, including working distance and spot size. The main variables, power and travel speed, were varied individually. Beam analysis was conducted using a PRIMES Focus Monitor to characterize the laser beam and a pro-beam diagnostic tool (PBD) for the electron beam. Electron beam welds were deflected or defocused to achieve a spot size similar to that of the laser welds, approximately 500 μm. The deflection pattern chosen for electron beam welding was made to mimic the power distribution of the laser. A similar melting efficiency at varying powers and travel speeds was maintained for both processes. Geometries and microstructures of the deflected and defocused electron beam welds and the laser beam welds are compared and related to process parameters.

Keywords Electron beam welding · Deflection pattern · Fiber laser welding · Austenitic stainless steel

1 Introduction

High energy density (HED) welds are useful for many highly critical joints in many industries including automotive [1], nuclear power [2], aerospace [1, 3], and medical devices [1, 4]. Desirable characteristics include high depth of penetration and depth/with ratio and low heat input. Welds which would require multiple passes using arc welding can often be completed in a single pass with reduced distortion and limited heat affected zone size. Often times, these welds are difficult to inspect using conventional non-destructive evaluation (NDE) techniques. Thus, the ability to predict weld penetration characteristics

---

✉ Joris E. Hochanadel
hochanadel.4@buckeyemail.osu.edu

1 The Ohio State University, Columbus, OH, USA

2 Los Alamos National Laboratory, Los Alamos, NM, USA

based on input parameters and material properties provides much greater utility for the "beam" processes.

Previous investigations have studied the influence of process parameters on the process and resulting weld characteristics. These have resulted in both computational and empirical models [5–12] that predict changes in weld profile and weld microstructure for both processes. Comparisons between high-power laser beam welding (LBW) and electron beam welding (EBW) have also been studied and generally show a higher depth of penetration for EBW [13]. This has widely been attributed to the coupling efficiencies, where EBW has a consistent coupling efficiency, or the efficiency of the beam that is absorbed by the material, of 90–95%, whereas LBW has efficiencies ranging from 30% in the conduction mode to 85% in keyhole mode welding [13, 14]. It should be noted that this is observed under hard vacuum conditions in EBW and atmospheric conditions for LBW. Vacuum effects can play a role in the ranges of efficiencies observed. Penetration characteristics in EBW have been generally understood much better than LBW since the interaction of electrons with metal is fundamentally simpler than the interaction of light radiation. For example, LBW must consider more complicated phenomena, including material-photon interactions, influence of the

laser plume, and the wide variety of coupling efficiencies based on material properties [13, 14]. Hann, et al. have investigated and mapped the effect of normalized parameters to determine depth of penetration for LBW [8, 9]. This and prior investigative work have made progress in the fundamental understanding of LBW. Elmer and Lippold have also investigated the effect of composition and solidification rate on the weld microstructure, which has resulted in the development of "microstructural maps" for austenitic stainless steels [11, 12] in both processes. A shift in solidification mode was observed in both processes at high solidification rates.

Thus, it is beneficial to compare the two processes in order to have greater fundamental knowledge of HED processes as well as to allow for process flexibility. The ultimate goal of this research is to develop an approach that allows the EBW and LBW processes to be used interchangeably and to provide better insight into the weld penetration characteristics and microstructure evolution that occurs in a range of structural materials, including steels, Ni-base alloys, and titanium alloys. This paper addresses some of these important issues regarding 304/304L stainless steel (Fig. 1).

2 Experimental procedures

Laser and electron beam bead-on-plate welds were performed on 304 and 304L stainless steel coupons. The compositions and WRC-1992 Cr/Ni equivalences for these materials are listed in Table 1 and plotted in Fig. 2. Composition was determined by optical emission spectrometry. The coupons to be welded were of the dimensions 0.19 × 6 × 12 in. (4.75 × 152.5 × 305 mm) for the 304 SS and 0.19 × 6 × 3 in. (4.75 × 152.5 × 76.2 mm) for the 304L SS. The length of each weld was 3 in. (76.2 mm). Two laser systems were used: an IPG YLS-4000

**Table 1** Composition and WRC-1992 Cr/Ni equivalences for the 304 and 304L SS

	Cr	Ni	Mn	Si	C	N	Mo	Cu	Fe	Cr/Ni
304	18.05	8.25	1.5	0.48	0.043	0.092	0.17	0.27	Bal.	1.56
304L	18.21	8.11	1.23	0.30	0.03	0.09		0.29	0.50	Bal.	1.67

was used for the 304 SS, and an IPG YLS-10000 was used for the 304L SS. One electron beam welder, a pro-beam K10 HVEBW machine, was used to perform welds. The parameters for the welds can be seen in Table 2. It should be noted that the range of parameters used were selected to observe a combination of high and low powers and travel speeds. Parameters which were kept constant, such as beam diameter and working distance, were used according to machine constraints. Optimization of parameters was not a concern in this study. Beam characterization was performed for the IPG YLS-10000 and the pro-beam K10 machines. A PRIMES Focus Monitor was used to characterize the laser beam, and a pro-beam diagnostic tool (PBD) was used to characterize the electron beam. It has been seen that the PBD produces comparable beam analysis to the enhanced modified Faraday cup, which is more commonly utilized, in work done by Pierce et al [14].

Welds were run keeping one of the parameters (power and travel speed) constant while varying one parameter of interest. The laser welds utilized argon shielding at a flow rate of 15 CFH, or 1.18 E-4 m^3/s, trailing. The electron beam chamber was pumped to a vacuum level which ranged from 5.2E-5 to 3.4E-4 torr. The coupons were clamped in each process to prevent distortion and therefore control beam diameter variations. The focusing and collimating lenses had lengths of 100 μm and 250 μm, respectively, for the YLS-4000 and

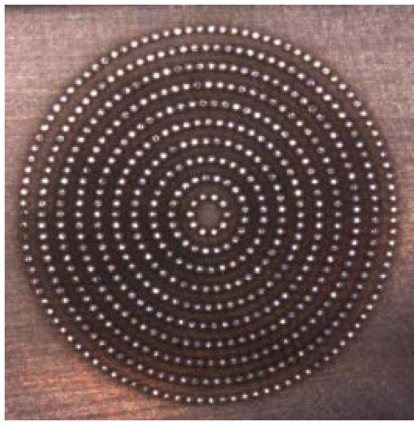**Fig. 1** WRC-1992 diagram showing location of materials. Red square: 304 SS, blue circle: 304L SS [13]
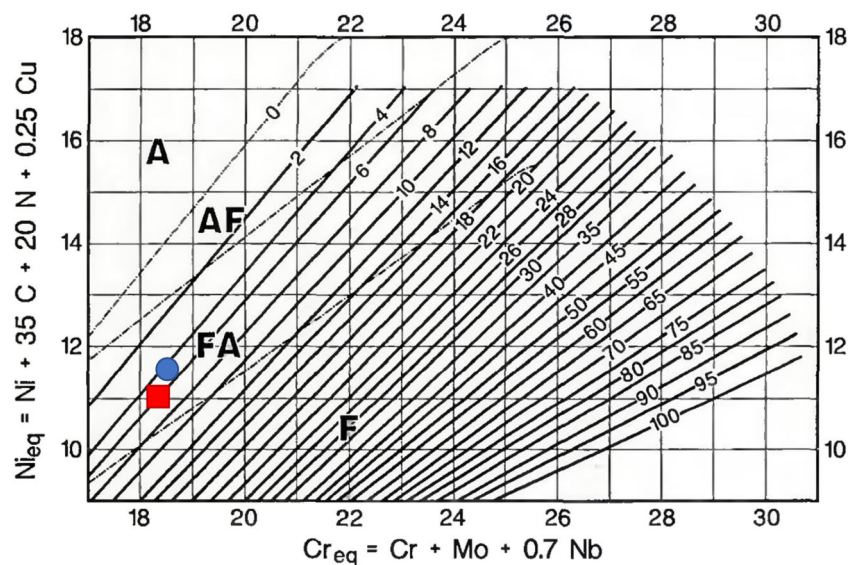
Fig. 2 Pro-beam "Fig. 6" deflection pattern [14]

150 μm and 250 μm, respectively, for the YLS-10000, and the optical fiber diameters were 200 μm and 300 μm, respectively, giving an ideal spot size of 500 μm. The electron beam had a narrower beam diameter ranging from 230 to 350 μm at sharp, so welds were made at both a defocused and deflected condition to achieve a similar spot size as the laser welds. The defocused condition was chosen to be overfocused and the deflected condition used a pattern known as "pro-beam figure 6," which used 1000 spots that were expanded and contracted in 10 concentric circles, as shown in Fig. 2. Previous work [15] has shown that this pattern can be used to "mimic" a top-hat distribution commonly seen in high-power fiber laser applications.

Welds were cross-sectioned, ground, polished, and etched in accordance with ASTM E407. The etchant used was 60% nitric acid in water, etched electrolytically. Weld macrographs were taken to document the weld penetration characteristics, and micrographs were taken to observe the weld microstructures. The results of the beam analysis, weld geometries, and weld microstructures are presented in the next section.

3 Results and discussion

3.1 Beam analysis

For the electron beam welds, the PBD was employed for 80, 85, 90, 100, and 110 kV and currents of 2, 4, 6, 8, 10, and 12

Table 2 Welding conditions

|	LBW	EBW
Power	400–2400 W	200–800 W
Travel speed	10–150 mm/s	20–90 mm/s
Working distance	207.5 mm	~ 208 mm
Target beam diameter	500 μm	

mA. It was seen that with an increase in current, the beam diameter also increased. As voltage increased, the beam diameter decreased slightly. This decrease was approximately 5 μm/10 kV at low currents and approximately 10 μm/10 kV at high currents. This is detailed in Fig. 3. Beam diameters were measured in terms of D_{86}, or the diameter where 86% of the intensity was concentrated. This was done automatically by the PBD software. More information for beam diameter measurements can be found in a paper by Burgardt et al [16]. The values of beam diameter at sharp focus were then used to determine the required deflection amplitude to achieve an effective spot size of 500 μm.

Spot size increases with increasing current because there are more electrons present, so the beam is not able to be constricted as much. Voltage had little influence because the focus current changed dramatically and was able to constrict the higher energy electrons to a similar diameter. The slight decrease in size is due to the increase in energy per electron, restricting the amount of time that the electrons repel each other. The map of the beam diameters at sharp focus is shown in Fig. 3. The defocused conditions were also determined using the PBD. Two runs were made at each condition: one with a large step size to determine a larger appearance of the beam and one with a smaller step size to get a finer determination of beam diameter at given foci. It was seen that current had negligible effects on focus, but changes in voltage displayed a large shift in focus current necessary to have a similar focal position. This is because the beam was at higher energy with higher voltages and required more restriction to achieve the same focal position. An example of the differences in beam characteristics can be seen in Fig. 4.

At sharp and overfocused conditions, the beam generally exhibited a standard Gaussian distribution. At the underfocused condition, however, it was seen that the beam resembled the filament, having a more square profile along with "hot spots" due to the corners of the filament conducting less heat out and therefore thermionically emitting more electrons. At sharp focus, the beam is at maximum constriction. This results in the electrons repelling uniformly in all directions which yields in a Gaussian distribution. For the defocused welds performed, the overfocused condition was chosen to have a more uniform distribution.

The laser diagnostics performed by PRIMES was performed for 700 to 1000 W with a step size of 100 W and 1000–2400 W with a step size of 200 W. The top-hat distribution was seen at sharp focus for all powers, which can be seen in Fig. 5. The D_{86} beam diameter ranged from 478 to 494 μm, with a slight increase as power rose to around 1000 W. This is likely due to the behavior of the laser at lower powers. Using the machine at the lower end of power capabilities results in less predictable behavior. Thermal lensing is not likely a concern. The chart of beam diameter vs power can be seen in Fig. 5.
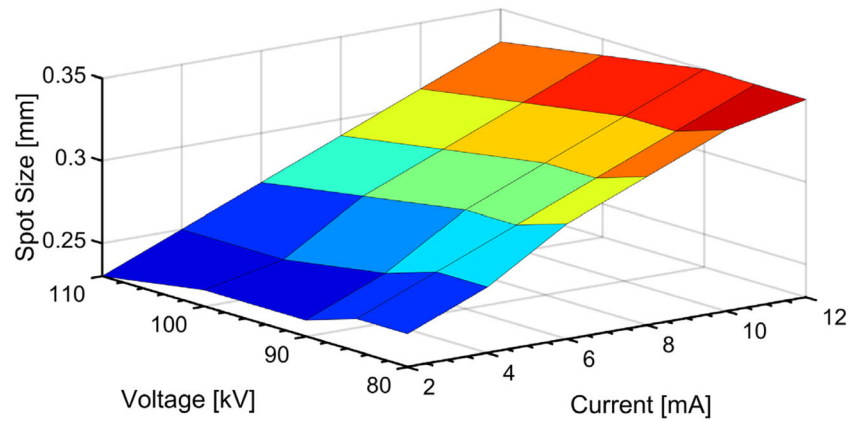
3.2 Weld geometries

The depth of penetration and fusion zone area were determined using a MATLAB code and plotted. Figures 6 and 7 show graphs of the depths of penetration and fusion zone areas for each condition comparing the 304 laser welds and the 304L electron beam welds. It can be seen that the sharp, deflected welds have the highest depth of penetration. The laser welds have the lowest. The defocused electron beam welds show slightly less penetration than the deflected welds. This is likely due to the scattering of the beam, which did not occur to that degree in the deflected condition. It should be noted that some 304 laser welds were performed under the same conditions as the 304L welds, and weld depth of penetration and fusion zone area show good agreement, so the 304 weld geometries are considered equivalent in this work, which is illustrated in Fig. 8.

The area of fusion for all conditions was found to follow the same trend, which suggests a similar melting efficiency. It should be noted that this is only true for the keyhole welds. According to Sudnik [17], melting efficiency can be defined as

$$\eta m = \frac{AFZ}{P} * v * C,$$

where ηm is the melting efficiency, A_{FZ} is the fusion zone area, P is power, v is travel speed, and C is a material constant defined by the material density times the enthalpy of melting. Rearranging this equation will allow the melting efficiency to be correlated to the slope of the graphs:

$$A_{FZ} = \eta m * \frac{P}{v} / C$$

Since the slope of the plot is linear for changing power and reciprocal for changing travel speed, the welds are in good agreement with this equation. It should be noted that this is only applicable for the keyhole mode welds. The low power and high travel speed laser welds were in conduction mode, so the melting efficiency is not the same. This similar melting efficiency is likely due to beam conditions. Once a keyhole was achieved, the electron beam and laser beam exhibited similar melting efficiencies since the laser did not have any losses due to beam manipulation. It should also be noted that these welds are not fit for service but analyzed to fundamentally determine process parameter-weld formation relationships. Reduced pore formation through process optimization was not the intent of this study, and it is likely that full penetration welds will substantially reduce pore formation.
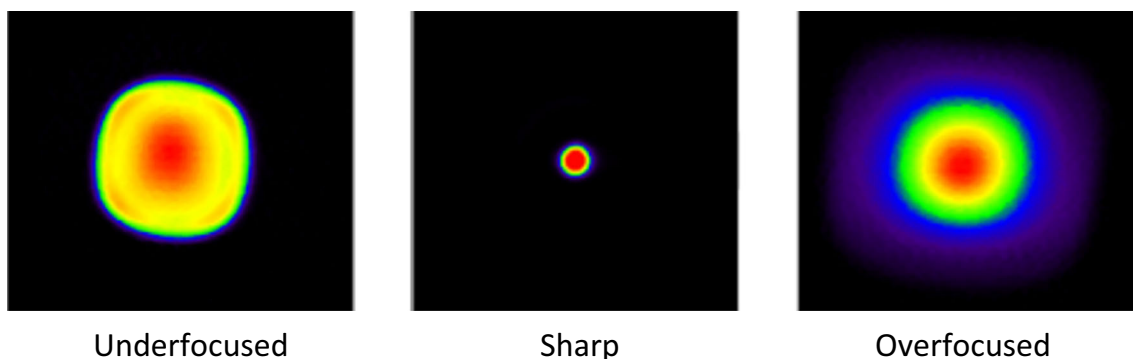

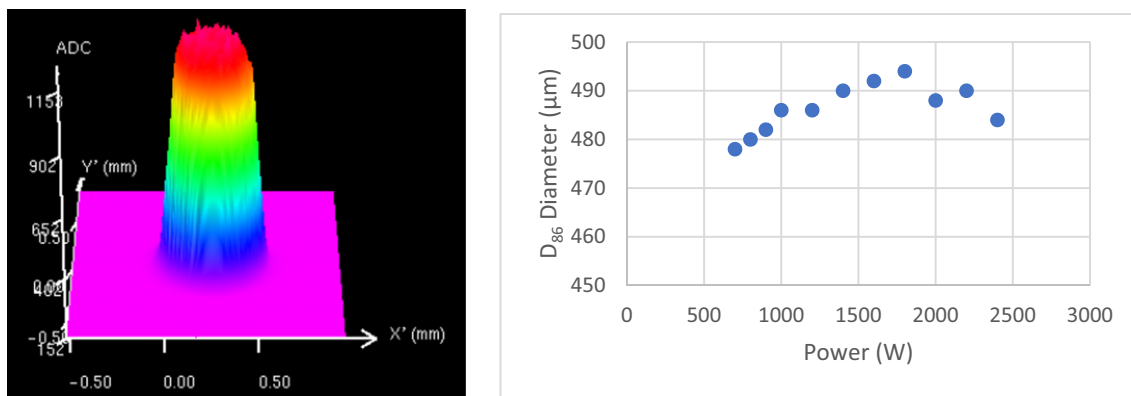**Fig. 4** Power distribution for different focus conditions of an electron beam

Fig. 5 Top-hat distribution for the laser beam at 1400 W (left) and variations in D_{86} diameter vs the power of the laser (right)

3.3 Weld microstructures

Representative microstructures from weld cross sections are shown in Fig. 9. All these micrographs are at the same magnification and were taken a roughly the same location at the mid-thickness of the weld. In general, all of the welds that were examined metallographically exhibited an FA (ferrite-austenite) solidification mode, resulting in a microstructure that is a mixture of ferrite (dark etching) and austenite. The solidification substructure is quite refined and shows a cell (or
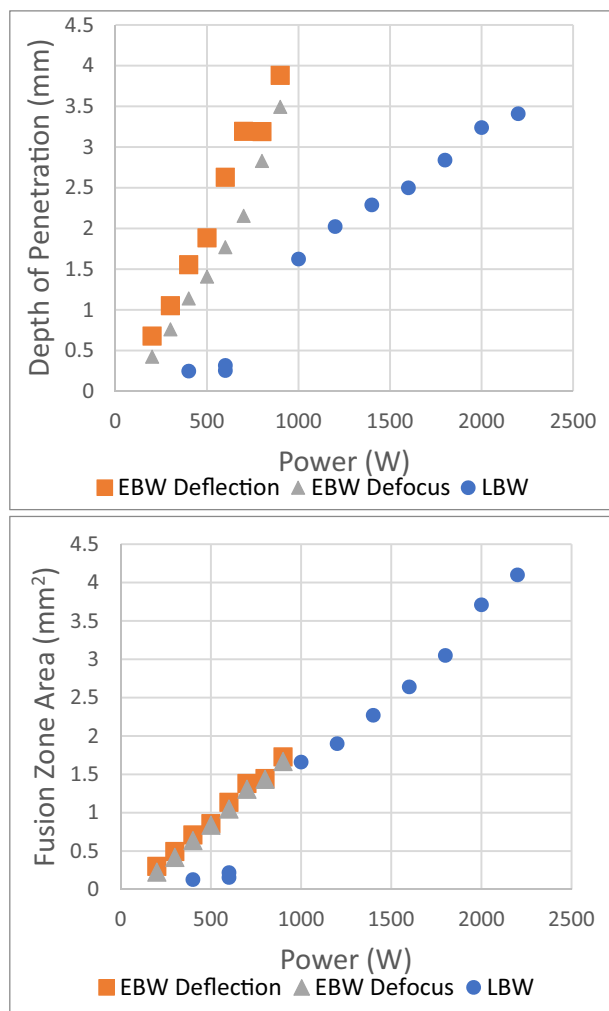
Fig. 6 Weld depth of penetration and fusion zone area with varying power. 25 mm/s travel speed. Scale bar applicable to each weld. Constant travel speed, varying power. TS: 25 mm/s, EBW voltage: 100 kV
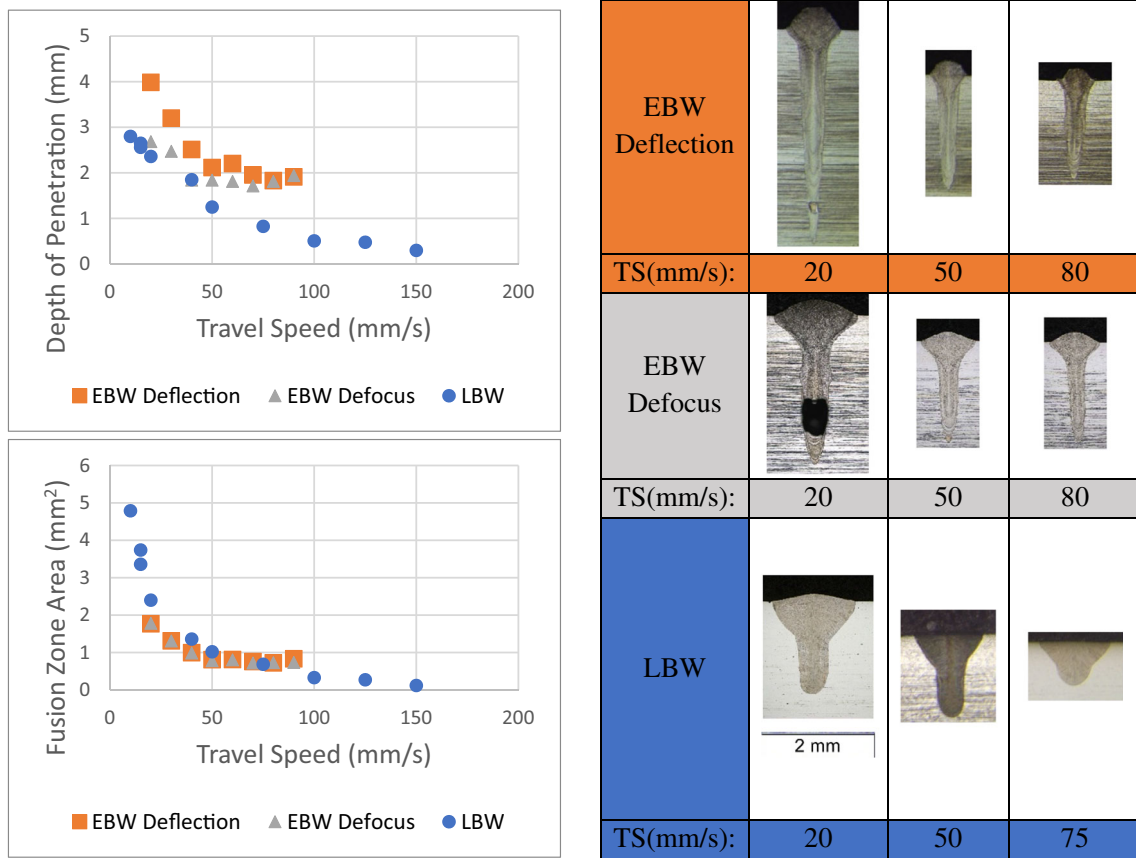
Fig. 7 Weld depth of penetration and fusion zone area with varying travel speed. 800 W power for EBW, 1400 W power for LBW. Scale bar applicable to each weld. Constant power, varying travel speed, EBW voltage: 100 kV

dendrite) spacing that is on the order of 10 microns. The ferrite morphology is predominantly skeletal, but there is also some lathy ferrite present in some locations.

Based on the composition and WRC-1992 Cr_{eq}/Ni_{eq} for these alloys, solidification should occur in the FA mode under "normal" solidification and cooling conditions. Lippold [12] and others have shown that under very high solidification and cooling rate conditions, such as those experienced during pulsed laser welding, a shift in

solidification behavior can occur. Under such conditions, the primary solidification phase can shift from ferrite to austenite and result in a weld metal that is fully austenitic. It is also possible that an alloy with a Cr_{eq}/Ni_{eq} greater than 1.5 can solidify as ferrite, but that the ferrite can completely transform to austenite via a diffusionless "massive" transformation under extreme cooling conditions. These transitions in solidification and transformation behavior are shown in Fig. 10 [12].
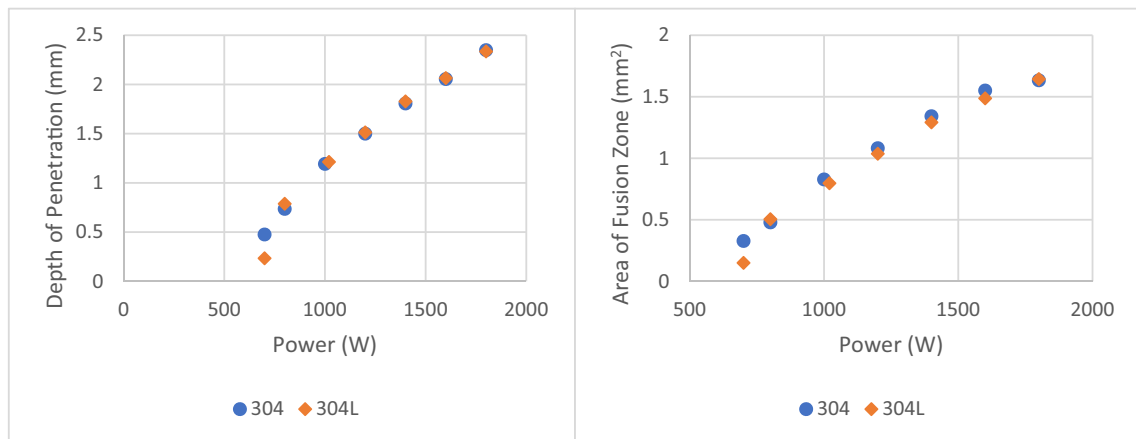

Fig. 8 304 (blue) vs 304L (orange) depth of penetration and fusion zone area vs power for LBW. Constant travel speed 50 mm/s

Fig. 9 Solidification structure of 304L SS. (**a**) EBW, 800 W, 25 mm/s. (**b**) EBW, 800 W, 80 mm/s. (**c**) LBW, 1000 W, 25 mm/s. (**d**) LBW, 1000 W, 100 mm/s. (**a**), (**b**), and (**c**) were keyhole mode welds, and (**d**) was conduction mode. Micrographs taken approximately at mid-thickness of each weld

a) EBW, 800 W, 25 mm/s

b) EBW, 800 W, 80 mm/s

c) LBW, 1000 W, 25 mm/s

d) LBW, 1000W, 100 mm/s
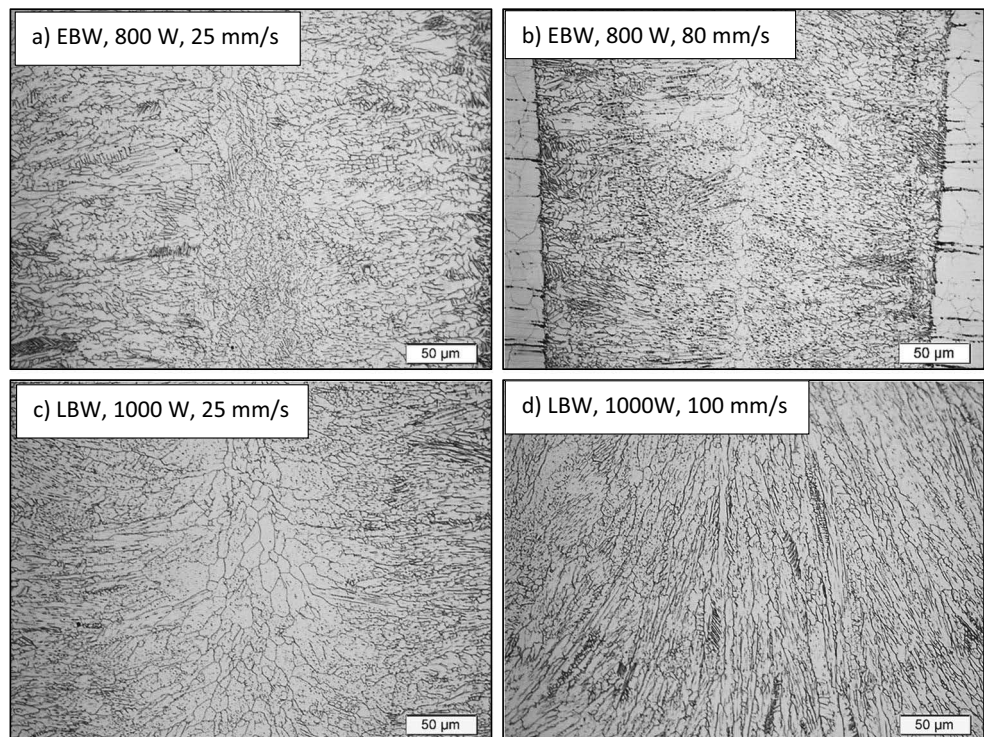
The location of the 304 and 304L alloys used in this study are superimposed on this diagram based on their Cr_{eq}/Ni_{eq} and expected range of solidification rates along the centerline that occur in the welds made in this study. The welds were assumed to experience steady state conditions in the middle of the weld, so the expected range of solidification rates along the centerline was assumed to be the travel speed. This diagram predicts that most of the fusion zone in the electron beam and laser beam welds reported here should undergo FA solidification and contain a mixture of ferrite and austenite. Based on the micrographs in Fig. 9, this appears to be the situation.

However, along the weld centerline where solidification rates are the highest (equal to the weld travel speed), the microstructure appears to be fully austenitic. The morphology of this austenite suggests that it formed via a massive transformation (F/MA) as would be predicted by Fig. 10, but a mixture of ferrite and austenite can be observed as the solidification rate decreases (away from the centerline). Additional characterization work, included the use of electron backscattered diffraction (EBSD) techniques, is underway to more accurately describe the nature of solidification and transformation behavior in these alloys under a range of EBW and LBW conditions.

Fig. 10 Pulsed laser weld microstructural map, from [12]. The red line represents the range of solidification rates experienced by the 304 welds at the centerline. The blue line represents the range of solidification rates experienced by the 304L welds at the centerline
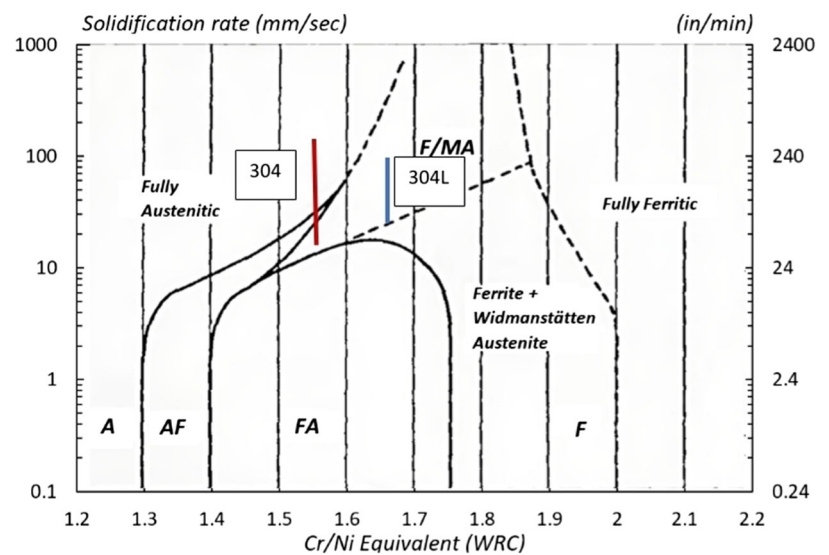
4 Conclusions

- Beam characterization was performed to determine parameters necessary for similar welding conditions between the two processes. Overfocused electron beams produced a more Gaussian distribution than underfocused beams. The underfocused beam produced a more irregular distribution with hot spots. Voltage had a large influence on focusing conditions, and current had a large influence on spot size at sharp. Laser beam characterization showed a slight increase in sharp spot size with increasing power, likely due to machine capabilities.

- Depth of penetration was significantly different between processes, but the area of fusion followed a similar trend. This suggests a similar melting efficiency between processes.

- The solidification and transformation trends in both alloys are consistent with the previous work with pulsed laser welding that showed variations in microstructure as a function of solidification and cooling rate.

References

1. Sánchez-Amaya JM, Pasang T, Amaya-Vazquez MR, De Dios Lopez-Castro J, Churiaque C, Tao Y, Botana Pedemonte FJ (2017) Microstructure and mechanical properties of Ti5553 butt welds performed by LBW under conduction regime. Metals 7(7). https://doi.org/10.3390/met7070269

2. Lin YD, Lee HT, Kuo TY, Jeng SL, Wu JL (2010) Effects of beam offset on mechanical properties and corrosion resistance of alloy 690-SUS 304L EBW joints for nuclear power plant. J Nucl Mater 401(1–3):78–85. https://doi.org/10.1016/j.jnucmat.2010.04.001

3. Oliveira JP, Schell N, Zhou N, Wood L, Benafan O (2019) Laser welding of precipitation strengthened Ni-rich NiTiHf high temperature shape memory alloys: microstructure and mechanical properties. Mater Des 162:229–234. https://doi.org/10.1016/j.matdes.2018.11.053

4. Shamsolhodaei A, Oliveira JP, Schell N, Maawad E, Panton B, Zhou YN (2020) Controlling intermetallic compounds formation during laser welding of NiTi to 316L stainless steel. Intermetallics 116(July 2019):106656. https://doi.org/10.1016/j.intermet.2019.106656

5. Rai R, Burgardt P, Milewski JO, Lienert TJ, Debroy T (2009) Heat transfer and fluid flow during electron beam welding of 21Cr-6Ni-9Mn steel and Ti-6Al-4V alloy. Journal of Physics D: Applied Physics 42(2). https://doi.org/10.1088/0022-3727/42/2/025503

6. Rai R, Elmer JW, Palmer TA, Debroy T. Heat transfer and fluid flow during keyhole mode laser welding of tantalum, Ti-6Al-4V, 304L stainless steel and vanadium

7. Kaplan A (1994) A model of deep penetration laser welding based on calculation of the keyhole profile. J Phys D Appl Phys 27(9):1805–1814

8. Hann DB, Iammi J, Folkes J (2011) A simple methodology for predicting laser-weld properties from material and laser parameters. Journal of Physics D: Applied Physics 44(44). https://doi.org/10.1088/0022-3727/44/44/445401

9. Hann DB, Iammi J, Folkes J (2010) Keyholing or conduction – prediction of laser penetration depth. Proc 36th Int MATADOR Conf 22(0):275–278

10. Suder WJ, Williams SW (2012) Investigation of the effects of basic laser material interaction parameters in laser welding. J Laser Appl 24(3):1–10

11. Elmer JW, Allen SM, Eagar TW (2007) Microstructural development during solidification of stainless steel alloys. Metall Trans A 20A(October):2117–2131, 1989. J. Phys. D. Appl. Phys., vol. 40, no. 18, pp. 5753–5766

12. Lippold JC (1994) Solidification behavior and cracking susceptibility of pulsed-laser welds in austenitic stainless steels A shift in solidification behavior under rapid solidification conditions promotes an increase in cracking susceptibility. Weld J 73(6):129–139

13. Kotecki DJ, Siewart TA (1992) WRC-1992 Constitution Diagram for Stainless Steel Weld Metals: A Modification of the WRC-1988 Diagram. Welding Journal 5:171s–178s

14. Pierce SW, Burgardt P (2016) Comparison of beam defocus and beam oscillation for Ta-10W EB welding. United States. Web

15. Pierce SW, Burgardt P (2014) Evaluation of two devices for electron beam profiling. United States. Web

16. Burgardt P, Pierce SW, Dvornak MJ. Definition of beam diameter for electron beam welding. United States: N. p., 2016. Web. https://doi.org/10.2172/1241647

17. Sudnik W (2011) Arc welding. InTech, Rijeka